ACCEPTED VERSION

Cheryl Suwen Law, Siew Yee Lim, Lina Liu, Andrew D. Abell, Lluis F. Marsal, and Abel Santos
Realization of high-quality optical nanoporous gradient-index filters by optimal combination of anodization conditions

---

PERMISSIONS

http://www.rsc.org/journals-books-databases/journal-authors-reviewers/licences-copyright-permissions/#deposition-sharing

Deposition and sharing rights

When the author accepts the licence to publish for a journal article, he/she retains certain rights concerning the deposition of the whole article. This table summarises how you may distribute the accepted manuscript and version of record of your article.

Sharing rights	Accepted manuscript	Version of record
Share with individuals on request, for personal use	✓	✓
Use for teaching or training materials	✓	✓
Use in submissions of grant applications, or academic requirements such as theses or dissertations	✓	✓
Share with a closed group of research collaborators, for example via an intranet or privately via a scholarly communication network	✓	✓
Share publicly via a scholarly communication network that has signed up to STM sharing principles	⧗	✕
Share publicly via a personal website, institutional repository or other not-for-profit repository	⧗	✕
Share publicly via a scholarly communication network that has not signed up to STM sharing principles	✕	✕

⧗ Accepted manuscripts may be distributed via repositories after an embargo period of 12 months

17 May 2021

---

http://hdl.handle.net/2440/124849

Nanoscale

Accepted Manuscript

Volume 10
Number 4
28 January 2018
Pages 1549-2172

Nanoscale

rsc.li/nanoscale

ISSN 2040-3372

PAPER
Shuping Xu, Chongyang Liang et al.
Organelle-targeting surface-enhanced Raman scattering
(SERS) nanosensors for subcellular pH sensing

ROYAL SOCIETY
OF CHEMISTRY

NCNST
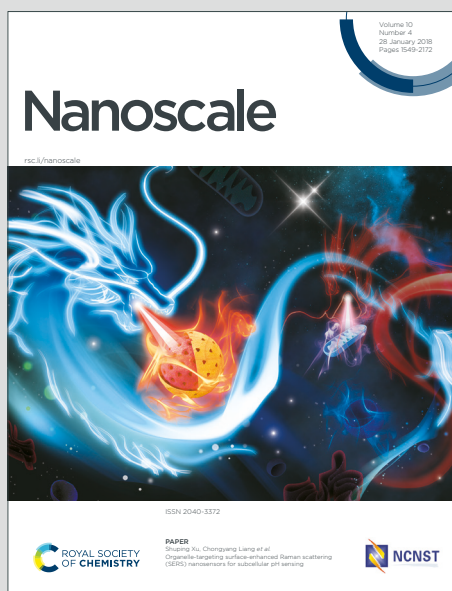
This is an Accepted Manuscript, which has been through the Royal Society of Chemistry peer review process and has been accepted for publication.

Accepted Manuscripts are published online shortly after acceptance, before technical editing, formatting and proof reading. Using this free service, authors can make their results available to the community, in citable form, before we publish the edited article. We will replace this Accepted Manuscript with the edited and formatted Advance Article as soon as it is available.

You can find more information about Accepted Manuscripts in the Information for Authors.

Please note that technical editing may introduce minor changes to the text and/or graphics, which may alter content. The journal's standard Terms & Conditions and the Ethical guidelines still apply. In no event shall the Royal Society of Chemistry be held responsible for any errors or omissions in this Accepted Manuscript or any consequences arising from the use of any information it contains.

Nanoscale

PAPER

Realization of High-Quality Optical Nanoporous Gradient-Index Filters by Optimal Combination of Anodization Conditions†

Cheryl Suwen Law[a,b,c], Siew Yee Lim[a,b,c], Lina Liu[a,d,e], Andrew D. Abell[*b,c,f], Lluis F. Marsal[*g] and Abel Santos[*a,b,c]

High-quality nanoporous anodic alumina gradient-index filters (NAA-GIFs) are realized by sinusoidal pulse anodisation (SPA) of aluminum. A three-level factorial design of experiments is used to determine the effect of three critical anodization parameters –electrolyte temperature, concentration of electrolyte and anodization time– on the quality of light control in these photonic crystal (PC) structures. Quantitative analysis of the effect of these anodization parameters on the quality of the characteristic photonic stopband (PSB) of NAA-GIFs reveals that all three anodization parameters and their respective combinations have statistically significant effects. However, anodization time is found to have the highest impact on the quality of light control in NAA-GIFs, followed by the electrolyte concentration and its temperature. Our findings demonstrate that NAA-GIFs fabricated under optimal conditions achieve an outstanding quality factor of ~86 (i.e. ~18% superior than that of other NAA-based PCs reported in the literature). This study provides a new insights onto optimal anodization conditions to fabricate high-quality NAA-based PC structures, opening new exciting opportunities to integrate these nanoporous PCs as platform materials for light-based technologies requiring a precise control over photons such ultra-sensitive optical sensors and biosensors, photocatalysts for green energy generation and environmental remediation, optical encoding and lasing.

Introduction

Nanoporous anodic alumina (NAA) films fabricated by anodization –electrochemically driven oxidation– of aluminum have been extensively researched for metal finishing applications such as surface finishing and decoration, automobile engineering, corrosion protection and wear resistance.[1] Fundamental aluminum anodization technology underwent breakthrough developments after the seminal works by Masuda and co-workers introducing the two-step anodization process –anodization approach that makes it possible to fabricate self-ordered NAA structures under mild anodization (MA) conditions (i.e. moderate electrolyte temperature and anodizing voltage/current density).[2–4] This milestone discovery boosted intensive research activity in NAA technology, spreading the applicability of this unique nanomaterial across multiple disciplines such as nanofabrication[5,6], separation and filtration[7,8], electromagnetism[9,10], chemo- and biosensing[11,12], photonics[13,14] and electronics[15,16]. Since then, numerous studies explored various anodization strategies and conditions to tailor-engineer the nanoporous structure of NAA for specific applications.[17] The pioneering works by Lee and co-workers on hard anodization (HA) and MA-HA pulse-like anodization opened new opportunities to directly and precisely translate anodizing voltage or current density pulses into in-depth modulations of nanopore diameter in NAA.[18–23] Pulse-like anodization was envisaged as an effective approach to overcome the electrically and ionically insulating nature of the oxide barrier layer located at the bottom of NAA.[24,25] However, MA-HA pulse anodization has limited controllability due to the fast and thickness-dependent nanopore growth rate under HA regime, and the extensive generation of Joule's heat, which often leads to catastrophic burning and cracking of the NAA film.[18]

Although less time-efficient, alternative pulse-like anodization performed under MA conditions provides much controlled conditions to modulate the inner porosity of NAA in depth.[26] This approach enabled exciting opportunities to generate a wide variety of NAA-based multi-dimensional photonic crystal (PC) structures. Recent efforts in pulse anodization have demonstrated the realization of NAA-PC structures such as multi-layered Fabry-Pérot interferometers (NAA-FPIs), distributed Bragg reflectors (NAA-DBRs), gradient-

a. School of Chemical Engineering and Advanced Materials, The University of Adelaide, Adelaide, South Australia 5005, Australia.

b. Institute for Photonics and Advanced Sensing, The University of Adelaide, Adelaide, South Australia 5005, Australia.

c. ARC Centre of Excellence for Nanoscale BioPhotonics, The University of Adelaide, Adelaide, South Australia 5005, Australia.

d. State key Laboratory of High-Efficiency Utilization of Coal and Green Chemical Engineering, Ningxia University, Yinchuan 750021, P. R. China.

e. College of Chemistry and Chemical Engineering, Ningxia University, Yinchuan 750021, P. R. China.

f. Department of Chemistry, The University of Adelaide, Adelaide, South Australia 5005 Adelaide, Australia.

g. Department of Electronic, Electric, and Automatics Engineering, University Rovira i Virgili, Tarragona, Tarragona 43007, Spain.

*E-Mails: andrew.abell@adelaide.edu.au ; lluis.marsal@urv.cat ; abel.santos@adelaide.edu.au

†Electronic supplementary information (ESI) available.

index filters (NAA-GIFs), bandpass filters (NAA-BPFs), optical microcavities (NAA-µCVs) and photonic tags.[27–34]

NAA-PCs are composite photonic structures made up of air and alumina (aluminum oxide – Al_2O_3).[26] The effective refractive index of NAA-PCs –average refractive index resulting from the relative fractions of NAA's individual components– can be engineered by a variety of pulse-like anodization strategies to generate specific structural arrangements for harnessing different forms of light–matter interactions (e.g. light confinement and recirculation, light filtering and lasing, light encoding).[26] Typically, the optical spectrum of NAA-PCs is characterized by a photonic stopband (PSB), which denotes those spectral regions within which light propagation is inhibited by the PC structure.[35–37] The intrinsic relationship between inner porosity and effective refractive index in NAA makes it possible to tailor-engineer the features of NAA-PCs' PSB (e.g. central wavelength position, full width at half maximum, intensity) by structural engineering via anodization. Spatial distributions of the refractive index of individual components in NAA-PCs (i.e. n_{air} = 1.00 RIU and n_{Al2O3} ~1.77 RIU) can be mechanistically described by different effective refractive index models such as Bruggeman, Maxwell–Garnett, Lorentz–Lorenz and Looyenga–Landau–Lifshitz.[38] Pulse anodization has been demonstrated as an optimal nanofabrication approach to modulate the PSB's features with versatility across the spectral regions –from UV to NIR– using a variety of pulse anodization modalities such as sinusoidal, stepwise, apodized sinusoidal and stepwise, and sawtooth.
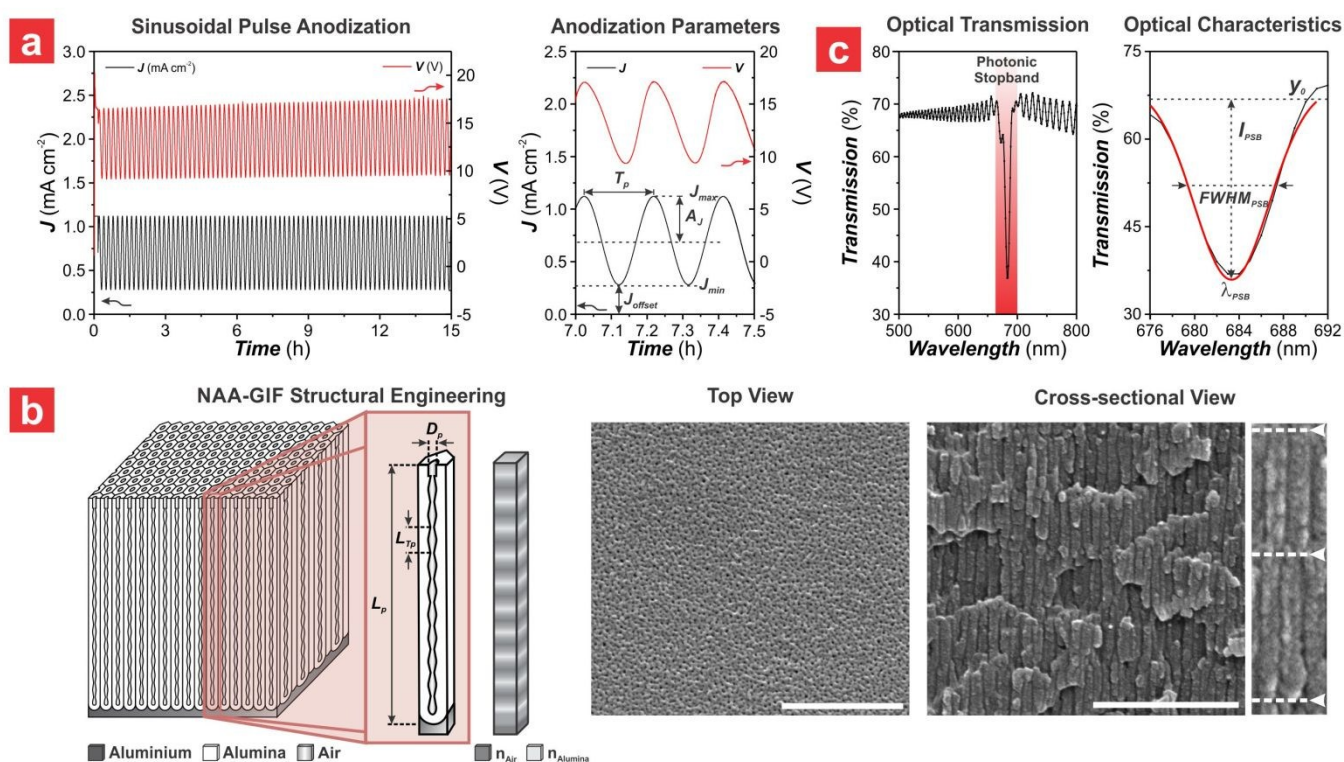

Fig. 1 Fabrication, structural composition and optical features of NAA-GIFs. (a) Representative sinusoidal pulse anodization (SPA) profile used to produce NAA-GIFs under current density control conditions (left), and graphical definition of anodization parameters (right) – current density amplitude (A_J), current density offset (J_{offset}), current density maximum (J_{max}), current density minimum or offset ($J_{min} = J_{offset}$) and anodization period (T_p) (NB: NAA-GIF fabricated with A_J = 0.420 mA cm^{-2}, J_{offset} = 0.280 mA cm^{-2} and T_p = 700 s in 1 M H_2SO_4 electrolyte at −2 °C for 15 h). (b) Illustration showing the idealized structure of NAA-GIFs with a graphical description of the main geometric features including period length (L_{Tp}), pore length (L_p) and pore diameter (D_p) (left), and representative top and cross-sectional FEG-SEM view images of a NAA-GIF with nanopore modulations in the magnified cross-sectional view (right) (NB: NAA-GIF fabricated with A_J = 0.420 mA cm^{-2}, J_{offset} = 0.280 mA cm^{-2} and T_p = 700 s in 1 M H_2SO_4 electrolyte at −2 °C for 15 h) (scale bar = 500 nm). (c) Optical transmission spectra of a representative NAA-GIF showing details of its photonic stopband (PSB) (left), and a graphical definition of its features – position of central wavelength (λ_{PSB}), full width at half maximum ($FWHM_{PSB}$), intensity (I_{PSB}) and baseline (y_0) (NB: NAA-GIF fabricated with A_J = 0.420 mA cm^{-2}, J_{offset} = 0.280 mA cm^{-2} and T_p = 700 s in 1 M H_2SO_4 electrolyte at −2 °C for 15 h).

Of all NAA-PCs structures, NAA-GIFs produced by sinusoidal pulse anodization feature a characteristically well-resolved, intense, narrow PSB associated with a smooth and periodic modulation of effective refractive index in depth, which is ~π/4 narrower than that of their quarter-wave NAA-DBR analogues.[39] Well-resolved and narrow PSBs are desirable for different light-based applications requiring a precise control over electromagnetic waves such as optical sensing and biosensing[11,12], optical encoding[40,41], lasing[42,43], light filtering[44,45] and photocatalysis[46–48]. Recent developments in pulse anodization technology have aimed at improving light control quality of NAA-PCs. Optimal structural engineering of NAA-µCVs has shown that these NAA-PCs can achieve outstanding light-confining capabilities, with resonance bands achieving unprecedented quality factors as high as 113[49] and 170[50]. A variety of sinusoidal pulse anodization strategies have

been explored to improve the quality of light control in NAA-GIFs, including implementation of apodization functions into anodization profiles[51] and application of anodizing voltage as a function of optical path length[52]. NAA-GIFs produced by these and other approaches have achieved high-quality PSBs, with quality factors of 27[53], 39[27], 43[54,55], 65[51] and 70[52].

Despite these advances, there remain fundamental and practical questions about rational design of pulse anodization conditions that can maximize the quality of light control in NAA-GIFs. In this scenario, we present a comprehensive study on the optimization of light control quality in NAA-GIFs produced by sinusoidal pulse anodization (SPA) (**Fig. 1a**). A three-level factorial design of experiments is used to determine and quantify the effect of three critical anodization parameters – anodization time, electrolyte temperature and concentration of electrolyte– on the PBS's quality of NAA-GIFs (**Fig. 1b**). The effect of these anodization parameters and their respective combinations on the optical features the characteristic PSB of NAA-GIFs (i.e. position of central wavelength, full width at half maximum, intensity, quality factor) is quantified and statistically assessed (**Fig. 1c**). This study provides new insights into anodization conditions for producing high-quality NAA-PCs, opening new opportunities to spread the applicability of these PC structures across a variety of light-based technologies.

Experimental Section

Materials

Al foils (99.9997% purity and 0.32 mm thick) were supplied by Goodfellow Cambridge Ltd. (UK). Perchloric acid ($HClO_4$), copper (II) chloride ($CuCl_2$), hydrochloric acid (HCl) and phosphoric acid (H_3PO_4) were supplied by Sigma-Aldrich (Australia). Sulfuric acid (H_2SO_4) and ethanol (EtOH, C_2H_5OH) were purchased form ChemSupply (Australia). All the chemicals were used as received, without further purification steps. Aqueous solutions used in this study were prepared with ultrapure Milli-Q® water (18.2 MΩ cm).

Fabrication of NAA-GIFs

NAA-GIFs were produced by SPA under current density control conditions.[56] Before anodization, 2.25 cm^2 square Al chips were sonicated in ethanol and water for 15 min each, dried under air stream, and electropolished in a mixture of EtOH and $HClO_4$ 4:1 (*v:v*) at 20 V and 5 °C for 3 min. Electropolished Al chips were anodized in an electrochemical reactor with controlled temperature and stirring rate (~300 rpm), using aqueous solutions of H_2SO_4 as acid electrolyte. The composition of the electrolyte was modified with 25 *v*% of EtOH to prevent it from freezing at sub-zero temperatures.[57,58] The electrolyte temperature was kept constant during anodization, using custom-built cold plate systems connected to high-performance refrigerated circulators model AC150-A25 (Thermo Fisher Scientific, Australia). The SPA process started with a constant current density step at 1.120 mA cm^{-2} for 10 min to form a thin nanoporous oxide layer and achieve a homogeneous pore growth rate prior to SPA. The anodization process was then switched to SPA mode, where the current density was sinusoidally pulsed between high (J_{max} = 1.120 mA cm^{-2}) and low ($J_{min} = J_{offset}$ = 0.280 mA cm^{-2}) levels. Current density–time SPA profiles were generated by a custom-designed LabVIEW®-based software according to **Eq. 1**, using Keithley 2400C and 2612B sourcemeters (Keithley Instruments, USA):

$$J(t) = A_J \times \left[sin\left(\frac{2\pi}{T_P} \times t\right) + 1 \right] + J_{offset} \qquad (1)$$

where $J(t)$ is the current density at a given time t, A_J is the current density amplitude, T_P is the anodization period (defined as the time between consecutive sinusoidal pulses), and J_{offset} is the current density offset (graphical description of the SPA parameters shown in **Fig. 1a**).

Table 1. Experimental matrix summarizing the fabrication conditions used to produce the nanoporous anodic alumina gradient-index filters (NAA-GIFs) assessed in this study.

t_{an} (h)	T_{an} (°C)	$[H_2SO_4]$ (M)			
		1.0	1.5	2.0	2.5
10	2	NAA-GIF$_{10,2,1.0}$	NAA-GIF$_{10,2,1.5}$	NAA-GIF$_{10,2,2.0}$	NAA-GIF$_{10,2,2.5}$
	0	NAA-GIF$_{10,0,1.0}$	NAA-GIF$_{10,0,1.5}$	NAA-GIF$_{10,0,2.0}$	NAA-GIF$_{10,0,2.5}$
	−2	NAA-GIF$_{10,−2,1.0}$	NAA-GIF$_{10,−2,1.5}$	NAA-GIF$_{10,−2,2.0}$	NAA-GIF$_{10,−2,2.5}$
15	2	NAA-GIF$_{15,2,1.0}$	NAA-GIF$_{15,2,1.5}$	NAA-GIF$_{15,2,2.0}$	NAA-GIF$_{15,2,2.5}$
	0	NAA-GIF$_{15,0,1.0}$	NAA-GIF$_{15,0,1.5}$	NAA-GIF$_{10,0,2.0}$	NAA-GIF$_{15,0,2.5}$
	−2	NAA-GIF$_{15,−2,1.0}$	NAA-GIF$_{15,−2,1.5}$	NAA-GIF$_{15,−2,2.0}$	NAA-GIF$_{15,−2,2.5}$
20	2	NAA-GIF$_{20,2,1.0}$	NAA-GIF$_{20,2,1.5}$	NAA-GIF$_{20,2,2.0}$	NAA-GIF$_{20,2,2.5}$
	0	NAA-GIF$_{20,0,1.0}$	NAA-GIF$_{20,0,1.5}$	NAA-GIF$_{20,0,2.0}$	NAA-GIF$_{20,0,2.5}$
	−2	NAA-GIF$_{20,−2,1.0}$	NAA-GIF$_{20,−2,1.5}$	NAA-GIF$_{20,−2,2.0}$	NAA-GIF$_{20,−2,2.5}$

Optimization of NAA-GIFs

To assess the effect of the main anodization parameters on the quality of NAA-GIFs, the anodization time (t_{an}), the electrolyte temperature (T_{an}) and its concentration ($[H_2SO_4]$), were systematically varied, from 10 to 20 h, from −2 to 2 °C, and from 1.0 to 2.5 M, respectively. **Table 1** summarizes the combination of fabrication conditions used to produce the NAA-

GIFs assessed in this study, with a total library of 36 NAA-GIFs labelled as NAA-GIF$_{tan,Tan,[H2SO4]}$ according to t_{an}, T_{an} and $[H_2SO_4]$. The rest of anodization parameters were fixed at A_J = 0.420 mA cm^{-2}, J_{offset} = 0.280 mA cm^{-2} and T_p = 700 s. The quality factor of NAA-GIFs' PSB –ratio of central wavelength position to its full width at half maximum– was used as the reference parameter

to assess the quality of light control in NAA-GIFs, as described in **Eq. 2**:

$$Q_{PSB} = \frac{\lambda_{PSB}}{FWHM_{PSB}} \qquad (2)$$

where λ_{PSB} is the PSB central wavelength position and $FWHM_{PSB}$ its full width at half maximum (graphical description shown in **Fig. 1c**).

An analysis of variance (ANOVA) for a three-level factorial design of experiments (DoE) was used to investigate both individual and combined effects of t_{an}, T_{an} and $[H_2SO_4]$ on the Q_{PSB} of NAA-GIFs, using the experimental matrix show in **Table 1**.[59] Seven null hypotheses with α_i, β_j and γ_k quantifying the effects of t_{an}, T_{an} and $[H_2SO_4]$ on Q_{PSB}, respectively, were tested by ANOVA as follows:

- (i) H_0, $\alpha_i = 0$ – there is no significant effect of t_{an} on Q_{PSB};
- (ii) H_1, $\beta_j = 0$ – there is no significant effect of T_{an} on Q_{PSB};
- (iii) H_2, $\gamma_k = 0$ – there is no significant effect of $[H_2SO_4]$ on Q_{PSB};
- (iv) H_3, $(\alpha \cdot \beta)_{ij} = 0$ – there is no significant effect of $t_{an} \cdot T_{an}$ interaction on Q_{PSB};
- (v) H_4, $(\alpha \cdot \gamma)_{ik} = 0$ – there is no significant effect of $t_{an} \cdot [H_2SO_4]$ interaction on Q_{PSB};
- (vi) H_5, $(\beta \cdot \gamma)_{jk} = 0$ – there is no significant effect of $T_{an} \cdot [H_2SO_4]$ interaction on Q_{PSB};
- (vii) H_6, $(\alpha \cdot \beta \cdot \gamma)_{ijk} = 0$ – there is no significant effect of $t_{an} \cdot T_{an} \cdot [H_2SO_4]$ interaction on Q_{PSB}.

If these hypotheses were rejected, the following alternative hypotheses would be accepted:

- (i*) H_0^*, $\alpha_i \neq 0$ – there is significant effect of t_{an} on Q_{PSB};
- (ii*) H_1^*, $\beta_j \neq 0$ – there is significant effect of T_{an} on Q_{PSB};
- (iii*) H_2^*, $\gamma_k \neq 0$ – there is significant effect of $[H_2SO_4]$ on Q_{PSB};
- (iv*) H_3^*, $(\alpha \cdot \beta)_{ij} \neq 0$ – there is significant effect of $t_{an} \cdot T_{an}$ interaction on Q_{PSB};
- (v*) H_4^*, $(\alpha \cdot \gamma)_{ik} \neq 0$ – there is significant effect of $t_{an} \cdot [H_2SO_4]$ interaction on Q_{PSB};
- (vi*) H_5^*, $(\beta \cdot \gamma)_{jk} \neq 0$ – there is significant effect of $T_{an} \cdot [H_2SO_4]$ interaction on Q_{PSB};
- (vii*) H_6^*, $(\alpha \cdot \beta \cdot \gamma)_{ijk} \neq 0$ – there is no significant effect of $t_{an} \cdot T_{an} \cdot [H_2SO_4]$ interaction on Q_{PSB}.

Optical Characterization of NAA-GIFs

Prior to optical characterization, a circular transparent window of ~5 mm in diameter was created on the backside of NAA-GIFs by selective chemical etching of the remaining aluminum substrate in a saturated solution of HCl–CuCl₂, using a Viton® etching mask. Transmission spectra of NAA-GIFs were acquired at normal incidence (i.e. $\vartheta = 0°$) from 200 to 800 nm with a resolution of 1 nm and a 5 nm slit, using a UV–visible spectrometer (Cary 300, Agilent, USA). Transmission spectra of NAA-GIFs were processed in OriginPro 8.5® to quantify the features of the characteristic PSB (i.e. λ_{PSB}, I_{PSB}, $FWHM_{PSB}$ and Q_{PSB}) from Gaussian fittings, using the upper lobe of the PSB as baseline (y_0). The interferometric color displayed by NAA-GIFs

was characterized by digital images acquired by a Canon EOS 700D digital camera equipped with a Tamron 90 mm F2.8 VC USD macro mount lens with an autofocus function under natural illumination, using a black background.

A set of NAA films produced under constant current density control conditions were used to characterize the effective refractive index of the different layers of NAA forming the structure of NAA-GIFs. These films were fabricated under the same conditions used to produce the most optimal NAA-GIFs (i.e. $T_{an} = -2$ °C, and $[H_2SO_4] = 1.0$ M) but at varying current density input, from 0.280 to 1.120 mA cm⁻² with $\Delta J = 0.210$ mA cm⁻². These NAA films were produced for a fixed total charge density (i.e. integrated current density per unit area and time) of 5 C cm⁻², and then left immersed in the H₂SO₄ electrolyte for a fixed time (i.e. 0, 5, 10, 15 and 20 h) after completion of anodization. Reflection spectra of these NAA films at varying angle of incidence ($\vartheta = 15°$, $25°$, $35°$ and $45°$) were acquired using a miniature visible optical fiber spectrometer (FLAME-T-VIS-NIR-ES, Ocean Optics, USA) coupled to a variable angle reflection stage (RSS-VA, Ocean Optics, USA) and to a tungsten light source (LS-1LL, Ocean Optics, USA) (schematic of setup system shown in **Fig. S1 – ESI**). NAA films were illuminated with white light over a spot size of ~2 mm in diameter, and reflected light was collected and guided to the miniature spectrometer by optical fibers (QP200-2-UV-VIS, Ocean Optics, USA). Reflection spectra were acquired from 400 to 900 nm, with an integration time of 10 ms and 20 average measurements, and processed by applying fast Fourier transform (FFT) using IgorPro® (Wavemerics, USA) to estimate the effective optical thickness (OT_{eff}) of these films according to **Eq. 3**:

$$OT_{eff} = 2n_{eff}L_p\cos\theta \qquad (3)$$

where OT_{eff} is the effective optical thickness of the NAA film, n_{eff} is its effective refractive index, L_p is its physical thickness and ϑ is the angle of incidence of light.

Structural Characterization

The structural features of NAA-GIFs and NAA films were characterized using a field emission gun scanning electron microscope (FEG-SEM FEI Quanta 450). FEG-SEM images were analyzed in ImageJ to establish the characteristic geometric features of NAA-GIFs.[60]

Results and Discussion

Fabrication and Structural Characterization of NAA-GIFs

Fig. 1b shows representative top and cross-sectional FEG-SEM images of NAA-GIFs fabricated in this study. Top view FEG-SEM images reveal a random but homogenous distribution of nanopores across the surface of NAA-GIFs, with an average nanopore diameter (D_p) of 9 ± 1 nm. The magnified cross-sectional view FEG-SEM image shows that the structure of NAA-GIFs is made of stacked layers of NAA, which correspond to each sinusoidal pulse in the SPA profile. The length of each NAA layer with sinusoidally modulated effective refractive index, defined as period length (L_{Tp}), is established by the anodization period (T_p) applied during the SPA process. FEG-SEM images analysis established a L_{Tp} of 0.17 ± 0.01 μm in NAA-GIFs fabricated with

T_p = 700 s, A_J = 0.420 mA cm^{-2} and J_{offset} = 0.280 mA cm^{-2} in 1.0 M H_2SO_4 electrolyte at –2 °C.

Qualitative Analysis of the Effect of t_{an}, T_{an} and $[H_2SO_4]$ on the Features of the PSB of NAA-GIFs

Fig. 2 shows the effect of the anodization time (t_{an}) on the optical transmission spectra of representative NAA-GIFs produced with T_p = 700 s, T_{an} = 0 °C, $[H_2SO_4]$ = 1.5 M and varying t_{an}, from 10 to 20 h with Δt_{an} = 5 h. The anodization conditions used in our study –highly concentrated sulfuric acid electrolyte at low temperature– enable the precise modulation of internal porosity of NAA by the sinusoidal current density input. The anodization profiles shown in **Figs. 2a–c** demonstrate that the current density input is translated into a voltage output that follows the input pattern precisely. Analysis of these anodization profiles reveals that, upon modification of the current density input, the voltage output undergoes a short recovery time (i.e. average recovery time ~4–20 s).[19] This is attributable to the enhanced ionic and electronic conductivity across the oxide barrier layer in highly concentrated H_2SO_4 electrolyte. Low electrolyte temperatures also minimize excessive dissolution of alumina during the anodization process. These conditions make it possible to achieve high control over porosity modulation without compromising the structural integrity of NAA-GIFs. FEG-SEM image of this set of NAA-GIFs (NAA-GIF$_{10,0,1.5}$, NAA-GIF$_{15,0,1.5}$ and NAA-GIF$_{20,0,1.5}$) reveals that the total thickness or pore length (L_p) of NAA-GIFs increases linearly at a rate of 1.12 ± 0.01 μm h^{-1} with t_{an}. NAA-GIFs produced with T_p = 700 s in $[H_2SO_4]$ = 1.5 M at T_{an} = 0 °C have total thicknesses of 11.2 ± 0.6, 16.8 ± 0.8 and 22.4 ± 1.1 μm h^{-1} for t_{an} = 10, 15 and 20 h, respectively (**Table 2**).
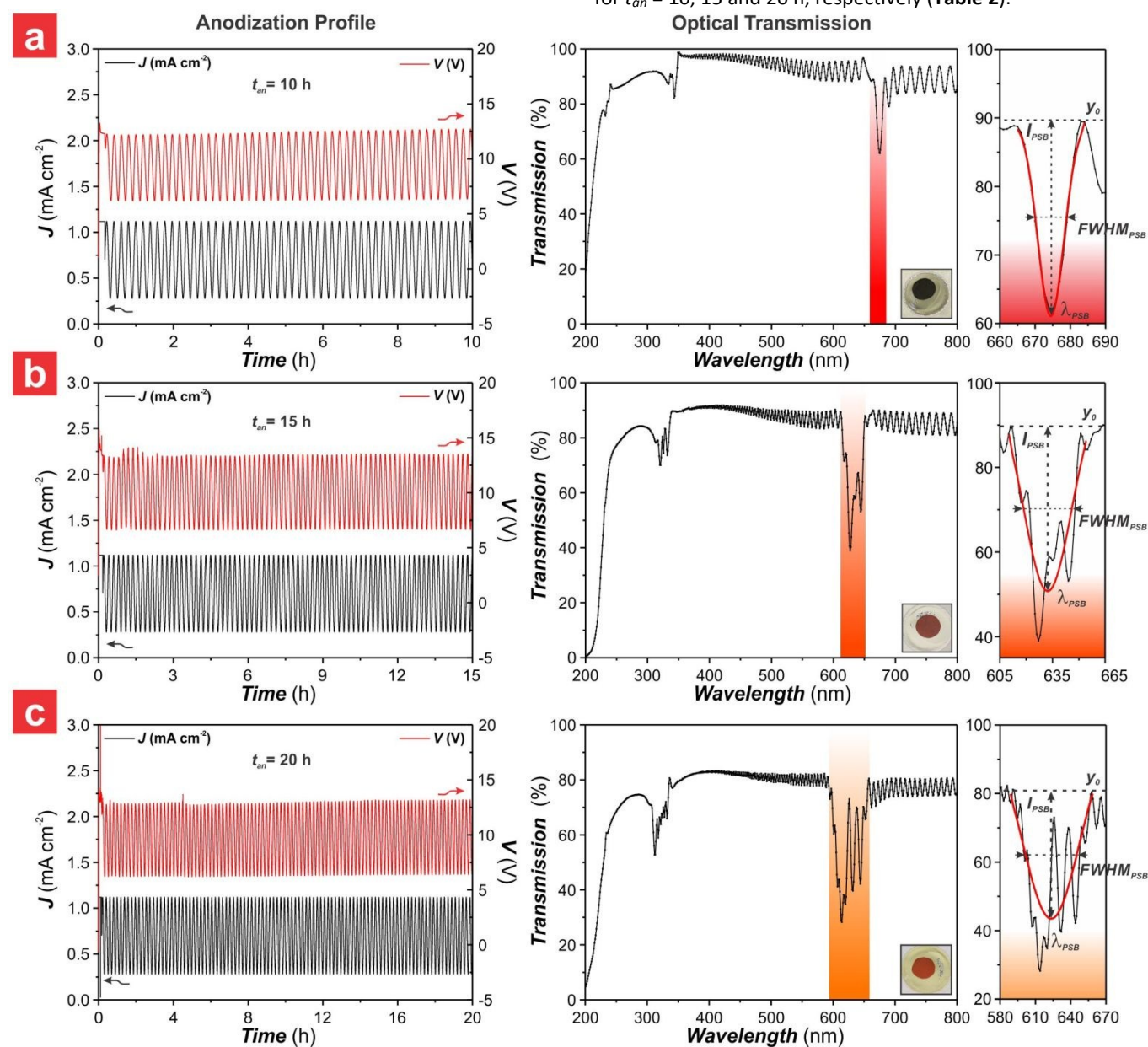

Fig. 2 Anodization profiles (left) and full optical transmission spectra (center) of NAA-GIF$_{10,0,1.5}$, NAA-GIF$_{15,0,1.5}$ and NAA-GIF$_{20,0,1.5}$ produced with varying anodization time (t_{an}), with insets showing digital images with details of the interferometric color, and magnified view of the PSB of these NAA-GIFs with details of its optical features (right). (a) NAA-GIF$_{10,0,1.5}$ produced with t_{an} = 10 h. (b) NAA-GIF$_{15,0,1.5}$ produced with t_{an} = 15 h. (c) NAA-GIF$_{20,0,1.5}$ produced with t_{an} = 20 h.

From the optical transmission spectra shown in **Figs. 2a–c**, it is apparent that t_{an} has a significant effect on the characteristics of the PSB of NAA-GIFs. **Table 2** summarizes the main optical features of the PSB of NAA-GIF$_{10,0,1.5}$, NAA-GIF$_{15,0,1.5}$ and NAA-GIF$_{20,0,1.5}$ (i.e. λ_{PSB}, $FWHM_{PSB}$, I_{PSB} and Q_{PSB}). It is observed that λ_{PSB} blue-shifts its position exponentially with t_{an} ($\lambda_{PSB} = 618 + 830 \cdot e^{(-t_{an}/3.7)}$), with $\lambda_{PSB} = 674 \pm 7$, 632 ± 6 and 621 ± 6 nm for $t_{an} = 10$, 15 and 20 h, respectively. This analysis also indicates that $FWHM_{PSB}$ undergoes a linear broadening with increasing t_{an} at a rate of 3.5 ± 0.1 nm h^{-1}. $FWHM_{PSB}$ for NAA-GIF$_{10,0,1.5}$, NAA-GIF$_{15,0,1.5}$ and NAA-GIF$_{20,0,1.5}$ estimated from Gaussian fittings shown in **Figs. 2a–c** were 8.8 ± 2.1, 27.0 ± 1.3 and 44.2 ± 2.2 nm, respectively. The anodization time also affects the intensity of the PSB in NAA-GIFs, increasing from 28.4 ± 1.4 to $43.1 \pm 2.2\%$ for $t_{an} = 10$ and 15 h, and slightly decreasing from 43.1 ± 2.2 to $37.9 \pm 1.9\%$ when t_{an} is extended from 15 to 20 h. Analysis of the quality factor of these NAA-GIFs reveals that, in principle, short anodization times are more suitable to achieve high Q_{PSB} values. NAA-GIF$_{10,0,1.5}$, NAA-GIF$_{15,0,1.5}$ and NAA-GIF$_{20,0,1.5}$ achieve Q_{PSB} values of 76.7 ± 3.8, 23.5 ± 1.9 and 14.0 ± 1.7, respectively. For this set of NAA-GIFs, Q_{PSB} decreases exponentially with t_{an} according to $Q_{PSB} = 12 + 2031 \cdot e^{(-t_{an}/2.9)}$.

Table 2. Summary of total thickness (L_p), position of central wavelength (λ_{PSB}), full width at half maximum ($FWHM_{PSB}$), intensity (I_{PSB}) and quality factor (Q_{PSB}) of NAA-GIFs fabricated by SPA in $[H_2SO_4] = 1.5$ M and $T_{an} = 0$ °C, with varying anodization time ($t_{an} = 10$, 15 and 20 h).

Optical Feature	NAA-GIF		
	NAA-GIF$_{10,0,1.5}$	NAA-GIF$_{15,0,1.5}$	NAA-GIF$_{20,0,1.5}$
L_p (mm)	11.2 ± 0.6	16.8 ± 0.8	22.4 ± 1.1
λ_{PSB} (nm)	674.0 ± 6.7	632.1 ± 6.3	621.1 ± 6.2
$FWHM_{PSB}$ (nm)	8.8 ± 2.1	27.0 ± 1.3	44.2 ± 2.2
I_{PSB} (%)	28.4 ± 1.4	43.1 ± 2.2	37.9 ± 1.9
Q_{PSB}	76.7 ± 3.8	23.5 ± 1.9	14.0 ± 1.7

Fig. 3 presents a comprehensive summary of the combined effect of t_{an}, T_{an} and $[H_2SO_4]$ on the features of the characteristic PSB (i.e. λ_{PSB}, $FWHM_{PSB}$, I_{PSB} and Q_{PSB}) of NAA-GIFs produced by SPA (**Table 1**). **Figs. S2–S4 (ESI)** compile full optical transmission spectra of NAA-GIFs with details of their PSB as a function of these three fabrication parameters. **Fig. 3a** shows the combined effect of T_{an} and $[H_2SO_4]$ on the PSB of NAA-GIFs produced with $t_{an} = 10$ h. It is apparent that λ_{PSB} remains relatively constant, with a slight fluctuation around an average value of 689 ± 24 nm at the upper visible spectral range (~650–730 nm), within the range of T_{an} and $[H_2SO_4]$ (i.e. from −2 to 2 °C, and from 1.0 to 2.5 M, respectively). A slight blue shift in average λ_{PSB} is observed with increasing $[H_2SO_4]$, which can be attributed to a faster dissolution rate of alumina with increasing acid electrolyte concentration. However, it is not possible to discern any trend in λ_{PSB} with varying T_{an} from this graph. Qualitative analysis of the combined effect of T_{an} and $[H_2SO_4]$ on the $FWHM_{PSB}$ of NAA-GIFs produced with $t_{an} = 10$ h indicates that low electrolyte concentrations are more suitable fabrication conditions to

produce NAA-GIFs with narrow PSB. The average spectral width of the PSB is narrowed when the electrolyte concentration is increased from 1.0 to 1.5 M (i.e. average $FWHM_{PSB} = 18 \pm 5$ and 10 ± 2 nm, respectively), and it broadens with increasing $[H_2SO_4]$ from 1.5 to 2.5 M (i.e. average $FWHM_{PSB} = 10 \pm 2$ and 25 ± 16 nm, respectively). It is apparent that this broadening of the PSB is weak at low electrolyte temperatures ($T_{an} = -2$ and 0 °C) and significantly prominent at relatively high electrolyte temperatures ($T_{an} = 2$ °C). Highly concentrated acid electrolyte at high temperature increases the dissolution rate of Al$_2$O$_3$. The differential dissolution rate of NAA layers produced at different current density enhances the refractive index contrast between layers of NAA forming the structure of NAA-GIFs. As a result, incoming photons are scattered more efficiently as they flow through the PC structure, broadening the characteristic PSB.[60–61] This graph also reveals that the intensity of the PSB in the transmission spectrum of NAA-GIFs (I_{PSB}) is weak and remains relatively constant, with a narrow fluctuation around an average value of $24 \pm 7\%$. Analysis of the quality factor of NAA-GIFs produced at $t_{an} = 10$ h with varying T_{an} and $[H_2SO_4]$ indicates a maximum Q_{PBS} of 79.7 ± 4.0 at 0 °C and 2.0 M. It is apparent that $T_{an} = 0$ °C is the most optimal electrolyte temperature to achieve high Q_{PSB} for $[H_2SO_4] < 2.5$ M, with increasing Q_{PSB} from 1.0 to 2.0 M (i.e. $Q_{PSB} = 55.5 \pm 2.8$, 76.7 ± 3.8 and 79.7 ± 4.0 for $[H_2SO_4] = 1.0$, 1.5 and 2.0 M, respectively). However, at $T_{an} = 0$ °C the quality factor of NAA-GIFs is dramatically worsened when the electrolyte concentration is increased to 2.5 M, achieving a minimum value of to 19.4 ± 1.0. The quality factor of NAA-GIFs produced at $T_{an} = -2$ and 2 °C follows a similar trend, with a significant enhancement from 1.0 M to 1.5 M (i.e. maxima of $Q_{PSB} = 71.9 \pm 3.6$ and 53.1 ± 2.7, respectively) and a sharp decrement for $[H_2SO_4] > 1.5$ M. Qualitative analysis of the two main parameters establishing the quality factor of NAA-GIFs produced with $t_{an} = 10$ h (i.e. λ_{PSB} and $FWHM_{PSB}$) indicates that Q_{PSB} relies strongly on $FWHM_{PSB}$, since λ_{PSB} remains relatively constant under such T_{an} and $[H_2SO_4]$ conditions.

The effect of T_{an} and $[H_2SO_4]$ on the PSB of NAA-GIFs produced with $t_{an} = 15$ h is shown in **Fig. 3b**. It is apparent that λ_{PSB} remains relatively constant at an average value of 660 ± 37 nm, although its fluctuation within the range of T_{an} and $[H_2SO_4]$ is slightly higher and blue-shifted than that of NAA-GIFs produced with $t_{an} = 10$ h, as indicated by the average λ_{PSB} and its standard deviation. Analysis of $FWHM_{PSB}$ reveals that a combination of increasing T_{an} and $[H_2SO_4]$ broadens the PSB of NAA-GIFs. However, the effect of the acid electrolyte concentration on $FWHM_{PSB}$ is found to be much more significant with increasing T_{an}, following a linear increment with $[H_2SO_4]$ at $T_{an} = -2$ °C, and a gradually increasing exponential growth at $T_{an} = 0$ and 2 °C. Dependence of $FWHM_{PSB}$ on T_{an} and $[H_2SO_4]$ is stronger in NAA-GIFs produced with $t_{an} = 15$ h than that of their analogues fabricated with $t_{an} = 10$ h. This effect is attributable to a combination of extended exposure time to the electrolyte solution, and a faster dissolution rate of Al$_2$O$_3$ with increasing T_{an} and $[H_2SO_4]$. It is observed that I_{PSB} of NAA-GIFs produced with $t_{an} = 15$ h undergoes a slight linear increment with $[H_2SO_4]$ for $T_{an} = 2$ and 0 °C, with respective linear rates of 16.6 ± 1.2 and 1.0 ± 4.4 % M^{-1}, and a moderate decrement with $[H_2SO_4]$ for T_{an}

= −2 °C (i.e. −3.6 ± 5.3 % M$^{−1}$). NAA-GIFs produced with t_{an} = 15 h have an average I_{PSB} of 38 ± 7 %, which is a ~58 % superior than that estimated for their NAA-GIF counterparts fabricated with t_{an} = 10 h. Analysis of Q_{PSB} with varying T_{an} and $[H_2SO_4]$ indicates that NAA-GIFs fabricated with t_{an} = 15 h achieve an outstanding maximum Q_{PSB} of 85.5 ± 4.3 at −2 °C and 1.0 M.

However, increasing T_{an} and $[H_2SO_4]$ have a detrimental effect on Q_{PSB}. Increasing electrolyte temperature and concentration worsen the quality of the PSB dramatically due to excessive broadening of the PSB, which is attributable to over-etching of the NAA-GIF structure.
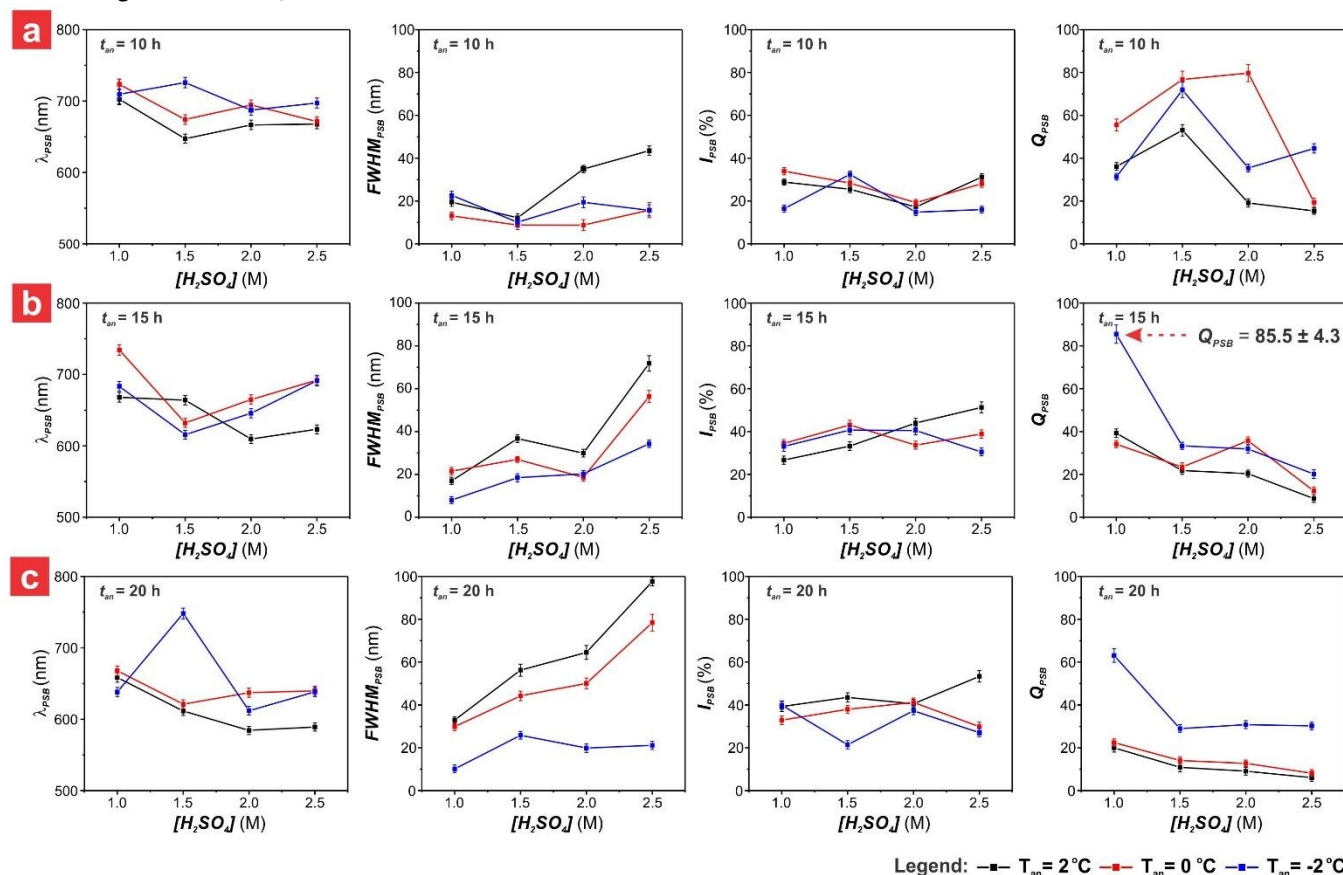
Fig.3 Combined effect of anodization time (t_{an} from 10 to 20 h), electrolyte temperature (T_{an} from −2 to 2 °C) and concentration ($[H_2SO_4]$ from 1.0 to 2.5 M) on the optical features of the PSB (position of central wavelength – λ_{PSB}; full width at half maximum – $FWHM_{PSB}$; intensity I_{PSB}; quality factor – Q_{PSB}) of NAA-GIFs produced by sinusoidal pulse anodization (SPA). (a) Combined effect of T_{an} and $[H_2SO_4]$ on the features of the PSB of NAA-GIFs fabricated with t_{an} = 10 h. (b) Combined effect of T_{an} and $[H_2SO_4]$ on the features of the PSB of NAA-GIFs fabricated with t_{an} = 15 h. (c) Combined effect of T_{an} and $[H_2SO_4]$ on the features of the PSB of NAA-GIFs fabricated with t_{an} = 20 h.

Fig. 3c describes the optical characteristics of NAA-GIFs fabricated with t_{an} = 20 h, and varying T_{an} and $[H_2SO_4]$. The PSB of these NAA-GIFs fluctuates across the yellow-orange spectral region (i.e. ~580–650 nm), with an average λ_{PSB} of 637 ± 43 nm. Qualitative analysis indicates that λ_{PSB} blue-shifts its position with increasing T_{an} and $[H_2SO_4]$. Comparison with NAA-GIFs produced with shorter anodization time (i.e. t_{an} = 10 and 15 h) reveals a higher fluctuation of λ_{PSB} around the average value of λ_{PSB} within the range of T_{an} and $[H_2SO_4]$. It is also confirmed that increasing anodization time blue-shifts λ_{PSB}, from 689 ± 24 nm to 637 ± 43 nm for t_{an} = 10 and 20 h, respectively. Analysis of the $FWHM_{PSB}$ of these NAA-GIFs indicates a dramatic broadening of the PSB with increasing $[H_2SO_4]$ at T_{an} = 0 and 2 °C, which becomes more prominent at higher electrolyte temperature. However, broadening of the PSB can be prevented when the electrolyte temperature is set at T_{an} = −2 °C, maintaining a narrow average $FWHM_{PSB}$ of 19.2 ± 6.6 nm for $[H_2SO_4]$ = 1.0–2.5 M. Qualitative analysis of I_{PSB} in NAA-GIFs

produced with t_{an} = 20 h reveals that an extended anodization time of 5 h does not have a significant impact on this optical parameter. The average I_{PSB} of NAA-GIFs fabricated with t_{an} = 20 h is 37.0 ± 8.3 %, which is statistically the same than that of their NAA-GIF counterparts produced with t_{an} = 15 h (i.e. 38 ± 7 %). The quality factor of NAA-GIFs fabricated with t_{an} = 20 h and varying T_{an} and $[H_2SO_4]$ shows a similar trend than that observed for NAA-GIFs fabricated with t_{an} = 15 h. NAA-GIFs fabricated with T_{an} = −2 °C and $[H_2SO_4]$ = 1.0 M achieve the highest Q_{PSB} (i.e. 63.1 ± 3.2) at t_{an} = 20 h. However, it is apparent that a combination of increasing T_{an} and $[H_2SO_4]$ worsens the quality of NAA-GIFs dramatically. It can also be observed that this effect is more prominent at higher T_{an}. Analysis of the average Q_{PBS} of NAA-GIFs produced with t_{an} = 20 h further demonstrates that extended anodization time worsens the quality of NAA-GIFs, with an average Q_{PBS} = 21.4 ± 15.9, which is ~52 % and ~30 % lower than that of NAA-GIFs fabricated with t_{an} = 10 and 15 h, respectively.

Another interesting optical property of NAA-GIFs is their interferometric color, which is associated with the position and intensity of their characteristic PSB. **Figs. 3 a–c** show that NAA-GIFs produced with t_{an} = 10–20 h, T_{an} = −2–2 °C and $[H_2SO_4]$ = 1.0–2.5 M feature a well-resolved PSB within the upper–middle range of the visible spectral region (i.e. ~585–750 nm). **Figs. 4a–c** compile a set of representative digital images of these NAA-GIFs. At first glance, it is apparent that NAA-GIFs produced with t_{an} = 10 h are transparent (**Fig. 4a**).
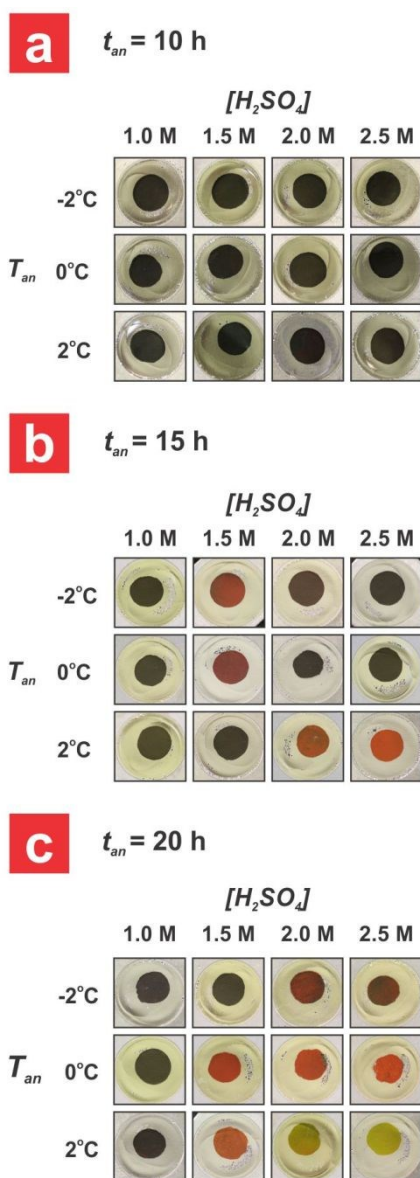

Fig. 4 Digital images of NAA-GIFs fabricated by SPA with varying anodization time (t_{an}), electrolyte temperature (T_{an}) and concentration ($[H_2SO_4]$). (a) NAA-GIFs produced with t_{an} = 10 h, and T_{an} = −2–2 °C and $[H_2SO_4]$ = 1.0–2.5 M. (b) NAA-GIFs produced with t_{an} = 15 h, and T_{an} = −2–2 °C and $[H_2SO_4]$ = 1.0–2.5 M. (c) NAA-GIFs produced with t_{an} = 20 h, and T_{an} = −2–2 °C and $[H_2SO_4]$ = 1.0–2.5 M.

Although the PSB of these NAA-GIFs is located within the upper section of the visible spectrum (λ_{PSB} ~650–730 nm), the intensity of the PSB is relatively weak (I_{PSB} = 24 ± 7%). As a result, light reflection by these PC structures is not efficient enough to generate interferometric color. **Fig. 4b** shows digital images of NAA-GIFs fabricated with t_{an} = 15 h, demonstrating that interferometric color raises with increasing anodization time. Some of these NAA-GIFs feature orange–red color (i.e. NAA-GIF$_{15,-2,1.5}$, NAA-GIF$_{15,0,1.5}$, NAA-GIF$_{15,2,2.0}$ and NAA-GIF$_{15,2,2.5}$). The position of the PSB of these PCs is also within the upper section of the visible spectrum (λ_{PSB} ~630–735 nm). However, the average intensity of the PSB of these NAA-GIFs (I_{PSB} = 38 ± 7 %) is higher than that of their NAA-GIF analogues produced with shorter anodization time. The interferometric color displayed by these NAA-GIFs is attributable to efficient reflection of incident light at those spectral regions that correspond with the position of the PSB. Digital images of NAA-GIFs fabricated with t_{an} = 20 h further confirm that interferometric color raises and achieves more vivid intensity with increasing t_{an} (**Fig. 4c**). NAA-GIFs produced with t_{an} = 20 h display vivid interferometric yellow, orange and red color, with the exception of NAA-GIF$_{20,-2,1.0}$, NAA-GIF$_{20,0,1.0}$, NAA-GIF$_{20,2,1.0}$ and NAA-GIF$_{20,-2,1.5}$, which are transparent. The PSB of these PCs is in the upper–middle section of the visible spectrum (λ_{PSB} ~580–650 nm), with an average I_{PSB} = 37.0 ± 8.3 %.

To summarize, qualitative analysis on the combined effect of t_{an}, T_{an} and $[H_2SO_4]$ on the optical features of the PSB of NAA-GIFs indicate that a combination of short t_{an} with low T_{an} and $[H_2SO_4]$ are more suitable anodization conditions to fabricate high quality NAA-GIFs. Our findings indicate that an optimal design of anodization conditions is critical to fabricating NAA-GIFs with high quality factors. Five NAA-GIFs fabricated in this study provide state-of-art quality factors, including NAA-GIF$_{10,-2,1.5}$, NAA-GIF$_{10,0,1.5}$, NAA-GIF$_{10,0,2.0}$, NAA-GIF$_{15,-2,1.0}$ and NAA-GIF$_{20,-2,1.0}$, with Q_{PSB} = 71.9 ± 3.6, 76.8 ± 4.0, 79.7 ± 4.0, 85.5 ± 4.3 and 63.1 ± 3.2, respectively.

Quantitative Analysis of the Effect of t_{an}, T_{an} and $[H_2SO_4]$ on the Quality of NAA-GIFs

A three-way analysis of variance (ANOVA) was used to statistically quantify the effect of t_{an}, T_{an} and $[H_2SO_4]$ on the quality of NAA-GIFs, using Q_{PSB} as reference variable. In this analysis, hypotheses H$_0$, H$_1$, H$_2$, H$_3$, H$_4$, H$_5$ and H$_6$ were assessed by comparing values of F_0 (i.e. test statistic calculated from ANOVA table; **Table S1 – ESI**) with the corresponding F-distribution values for a significance level of 95 %.[58] ANOVA results summarized in **Table 3** indicate that hypotheses H$_0$, H$_1$ and H$_2$ are rejected, since their individual F_0 values are much greater than those of their respective F-distribution, with F_{0-tan} = 1356.0 > $F_{0.05,2,72}$ = 2.4, F_{0-Tan} = 1032.3 > $F_{0.05,2,72}$ = 2.4, and $F_{0-[H2OS4]}$ = 816.3 > $F_{0.05,3,72}$ = 2.2. Therefore, their alternative hypotheses H$_0^*$, H$_1^*$ and H$_2^*$ are accepted, revealing that the individual effect of these anodization parameters over Q_{PSB} is statistically significant. Hypothesis H$_3$, H$_4$ and H$_5$ represent the two-way interactions between t_{an}, T_{an} and $[H_2SO_4]$ (i.e. $t_{an}\square T_{an}$, $t_{an}\square [H_2SO_4]$ and $T_{an}\square [H_2SO_4]$). ANOVA results also indicate that the combinations of these anodization parameters have a statistically significant effect on Q_{PSB}, as demonstrated by their respective F_0 values (i.e. $F_{0-tan\square Tan}$ = 312.3 > $F_{0.05,4,72}$ = 2.0, $F_{0-tan\square [H2SO4]}$ = 366.9 > $F_{0.05,6,72}$ = 1.9 and $F_{0-Tan\square [H2SO4]}$ =143.7 >

Nanoscale   **PAPER**

$F_{0.05,6,72}$ = 1.9). This suggests that hypotheses H_3, H_4, H_5 are rejected and thus the alternative hypotheses H_3^*, H_4^* and H_5^* are accepted. ANOVA results also demonstrate that the three-way interaction between t_{an}, T_{an} and $[H_2SO_4]$ (i.e. $t_{an} \cdot T_{an} \cdot [H_2SO_4]$)

is statistically significant (i.e. $F_{0-tan \cdot Tan \cdot [H2SO4]}$ = 121.0 > $F_{0.05,12,72}$ = 1.7) and therefore the alternative hypothesis H_6^* is accepted.

Table 3. Summary of ANOVA results for the evaluation of the statistical effect of individual, binary and ternary combinations of t_{an}, T_{an} and $[H_2SO_4]$ on the quality factor (Q_{PSB}) of NAA-GIFs produced by sinusoidal pulse anodization.

Source of Variance	t_{an} (h)	T_{an} (°C)	$[H_2SO_4]$ (M)	$t_{an} \cdot T_{an}$ (h·°C)	$t_{an} \cdot [H_2SO_4]$ (h·M)	$T_{an} \cdot [H_2SO_4]$ (°C·M)	$t_{an} \cdot T_{an} \cdot [H_2SO_4]$ (h·M·°C)	Model	Error
$SS^\dagger$	10085.7	7677.9	9107.7	4645.5	8187.7	3206.7	5400.2	48311.3	267.8
$DF^\dagger$	2	2	3	4	6	6	12	35	72
$MS^\dagger$	5042.9	3838.9	3035.9	1161.4	1364.6	534.4	450.0	1380.3	3.7
$F_0^\dagger$	1356.0	1032.3	816.3	312.3	366.9	143.7	121.0	371.2	–

$^\dagger SS$ = sum-of-squares; DF = degrees of freedom; MS = mean squares; F_0 = test statistic.

In summary, results from ANOVA reveal that t_{an}, T_{an} and $[H_2SO_4]$ have statistically significant effect on the quality factor of NAA-GIFs. However, t_{an} is found to be the most significant parameter in establishing Q_{PSB}, with a 32.7 % weight on the analyzed variable. T_{an} and $[H_2SO_4]$ also have statistically significant effect on Q_{PSB}, with a 24.9 and 19.7 % weight over this variable, respectively. Analysis of the effect of binary combinations between these anodization parameters demonstrates that $t_{an} \cdot [H_2SO_4]$ have the highest weight on Q_{PSB} (8.8 %), followed by $t_{an} \cdot T_{an}$ and $T_{an} \cdot [H_2SO_4]$ with 7.5 and 3.5 % weight, respectively. Finally, the ternary combination of anodization parameters (i.e. $t_{an} \cdot T_{an} \cdot [H_2SO_4]$) is found to be the weakest of all the analyzed effects, with a 2.9 % weight over the quality factor of NAA-GIFs. From these results, it is apparent that the effect of individual anodization parameters on Q_{PSB} is much more significant than that of their binary and ternary combinations.

Effect of Anodization Time on Effective Medium of NAA-GIFs

ANOVA results have demonstrated that anodization time is the most critical anodization parameter in determining the quality factor of NAA-GIFs produced by SPA. In this nanofabrication process, NAA-GIFs are exposed to the acid electrolyte for an extended period of time (t_{an}), during which the structure of NAA-GIFs is progressively etched due to dissolution of Al_2O_3 in acidic medium. The progressive widening of nanopores results in a differential effective optical thickness –product between effective refractive index and physical thickness– between top and bottom stacks of NAA forming the structure of NAA-GIFs. To assess the effect of t_{an} on the effective optical thickness of the NAA layers of NAA-GIFs produced under the most optimal anodization conditions (i.e. T_{an} = −2 °C and $[H_2SO_4]$ = 1.0 M), a set of NAA films was produced under constant current density at a fixed total charge density of 5 C cm^{-2} and varying current density input, from 0.280 to 1.120 mA cm^{-2} with ΔJ = 0.210 mA cm^{-2}. After fabrication, NAA films were exposed to the electrolyte solution for a fixed time (i.e. 0, 5, 10, 15 and 20 h) to mimic the range of t_{an} used in this study. The optical thickness (OT_{eff}) and effective refractive index (n_{eff}) of these NAA films were determined from FEG-SEM image analysis and by applying FFT to the reflection spectra of these NAA films at ϑ = 15°, 25°, 35° and 45° (**Figs. S1 and S5 – ESI**), respectively.
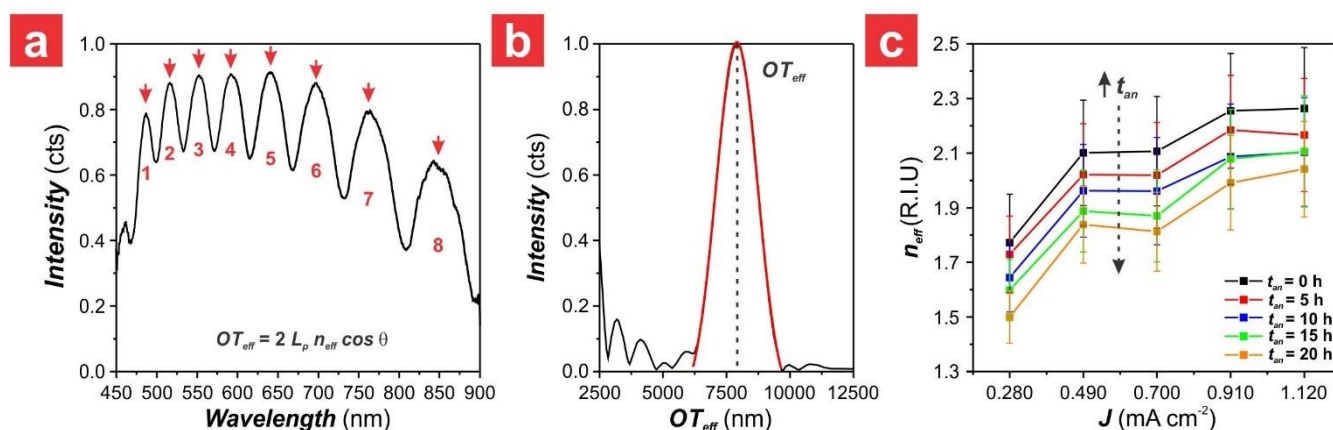

Fig. 5 Assessment of effective medium of NAA-GIFs as a function of anodizing current density (J = 0.280–1.120 mA cm^{-2}) and anodization time (t_{an} = 0–20 h) (NB: T_{an} = −2 °C and $[H_2SO_4]$ = 1.0 M). (a) Representative reflection spectrum of a NAA film fabricated with J = 1.120 mA cm^{-2} and t_{an} = 0 h at an incidence angle of 35° (NB: Fabry-Pérot interference oscillations are denoted by red arrows). (b) Estimation of effective optical thickness (OT_{eff}) of the representative NAA film by applying fast Fourier transform to the reflection spectrum shown in (a). (c) Effective refractive index (n_{eff}) of NAA films as a function of J and t_{an}.

Fig. 5a shows a representative reflection spectrum of an as-produced NAA film (i.e. t_{an} = 0 h) fabricated with J = 1.120 mA cm^{-2} at ϑ = 35°. The reflection spectrum of these films is characterized by well-resolved oscillations that follow an interference pattern associated with the Fabry-Pérot effect (**Eq. 3**). The OT_{eff} of NAA films can be estimated by applying FFT to

the reflection spectrum, as illustrated in **Fig. 5b**. **Fig. S1 (ESI)** shows the dependence of OT_{eff} with J, ϑ and t_{an}. It is apparent from these graphs that the effective optical thickness of NAA films decreases with increasing angle of incidence and anodization time, and increases with increasing anodizing current density. **Fig. 5c** shows the effective refractive index of these films as a function of J and t_{an}, which were calculated by **Eq. 3** using the estimated values of OT_{eff} and L_p obtained from FFT calculations and FEG-SEM image analysis, respectively. This graph reveals that n_{eff} follows a sigmoidal-like increment with increasing J, with a plateau between 0.490 to 0.700 mA cm^{-2}. It is also observed that n_{eff} decreases with increasing t_{an}. For instance, NAA films fabricated with J = 0.280 and 1.120 mA cm^{-2} have n_{eff} = 1.77 ± 0.018 and 2.26 ± 0.22 RIU at t_{an} = 0 h, and n_{eff} = 1.50 ± 0.10 and 2.04 ± 0.17 RIU at t_{an} = 20 h, respectively. This indicates that nanopores in these NAA films are widened upon extended exposure to the electrolyte solution. As a result, this progressive nanopore widening is translated into a differential reduction of the effective refractive index along the layers forming the structure of NAA-GIFs, worsening the quality factor of these PC structures during extended anodization time. This result further confirms the ANOVA results, in which anodization time is found to have the highest impact on the quality factor of NAA-GIFs.

Conclusions

In summary, this study has demonstrated the fabrication of high-quality nanoporous anodic alumina gradient-index filters by sinusoidal pulse anodization performed under optimized conditions. The individual and combined effects of three main anodization parameters –electrolyte temperature, concentration of electrolyte and anodization time– on the quality factor of NAA-GIFs have been systematically investigated in order to determine the most optimal anodization conditions to produce high-quality NAA-GIFs. A three-level factorial ANOVA analysis performed on the quality factor of NAA-GIFs has established that all three anodization parameters and their respective combinations have statistically significant effects on Q_{PSB}. However, anodization time is the most critical parameter in establishing the quality of NAA-GIFs, followed by the electrolyte concentration and its temperature. Although statistically significant, the effect of binary and ternary combinations of these anodization parameters are not as critical as that of their individual contributions. Analysis of optical spectra of NAA films upon exposure to acid electrolyte has revealed a progressive reduction of effective refractive index associated with nanopore widening due to dissolution of alumina. This gradual modification of effective refractive index along the layers forming the structure of NAA-GIFs worsens the quality factor of these PC structures upon extended anodization time. NAA-GIFs produced with an anodization time of 15 h, an anodization temperature of −2 °C and an electrolyte concentration of 1 M achieve an outstanding Q_{PSB} of 85.5 ± 4.3, with a well-resolved and narrow PSB with a $FWHM_{PSB}$ of 8.0 ± 1.6 nm, which are ~18 % higher and 20 % narrower than that of other state-of-the-art NAA-GIF structures. Despite these

advances, more fundamental research should be performed in order to establish optimal anodization conditions that can prevent NAA from partial dissolution during exposure to acid electrolytes. Such conditions, combined with advanced anodization strategies to compensate unbalanced effective optical thickness between NAA layers, will make it possible the realization of NAA-PCs with well-resolved, ultra-narrow PSBs.

We trust this study provides a strong foundation towards developing high-quality NAA-based photonic crystals, which could find broad applicability in light-based technologies requiring a precise control over electromagnetic waves such as optical sensing and biosensing, photocatalysis, optoelectronics and lasing.

Conflict of Interest

Authors have no conflict of interest to declare.

Acknowledgements

References

1. J.M. Runge, *The Metallurgy of Anodizing Aluminum*, Springer: Heidelberg, Germany, 2017.
2. H. Masuda and K. Fukuda, *Science*, 1995, **268**, 1466–1468.
3. H. Masuda, H. Hasegwa and S. Ono, *J. Electrochem. Soc.*, 1997, **144**, L127–L130.
4. H. Masuda, K. Yada and A. Osaka, *Jpn. J. Appl. Phys.*, 1998, **37**, L1340.
5. T. Yanagashita, K. Nishio and H. Masuda, *Adv. Mater.*, 2005, **17**, 2241–2243.
6. S.–J. Park, H. Han, H. Rhu, S. Baik and W. Lee, *J. Mater. Chem. C*, 2013, **1**, 5330–5335.
7. T. Yamashita, S. Kodama, T. Kemmei, M. Ohto, E. Nakayama, T. Muramoto, A. Yamaguchi, N. Teramae and N. Takayanagi, *Lab Chip*, 2009, **9**, 1337–1339.
8. T. Sano, N. Iguchi, K. Lida, T. Sakamoto, M. Baba and H. Kawaura, *Appl. Phys. Lett.*, 2003, **83**, 4438–4440.
9. J. Bachmann, J. Jing, M. Knez, S. Barth, H. Shen, S. Mathur, U. Gösele and K. Nielsch, *J. Am. Chem. Soc.*, 2007, **129**, 9554–9555.
10. K. Pitzschel, J.M. Montero–Moreno, J. Escrig, O. Albrecht, K. Nielsch, J. Bachmann, *ACS Nano* 2009, **3**, 3463–3468.
11. C.S. Law, S.Y. Lim, A. Abell, N. Voelcker and A. Santos, *Nanomaterials*, 2018, **8**, 788.

12. A. Santos, T. Kumeria and D. Losic, *TrAC, Trends Anal. Chem.*, 2013, **44**, 25–38.

13. H. Masuda, M. Ohya, H. Asoh, M. Nakao, M. Nohtomi and T. Tamamura, *Jpn. J. Appl. Phys.*, 1999, **38**, L 1403.

14. H. Masuda, M. Ohya, K. Nishio, H. Asoh, M. Nakao, M. Nohtomi, A. Yokoo and T. Tamamura, *Jpn. J. Appl. Phys.*, 2000, **39**, L 1039.

15. Y.B. Shin, W.Y. Kim and H.C. Lee, *J. Microelectromech. Syst.*, 2019, **28**, 1032–1038.

16. G.J. Jeon, W.Y. Kim and H.C. Lee, *Microelectron. Eng.*, 2013, **103**, 99–105.

17. W. Lee, S.–J. Park, *Chem. Rev.*, 2014, **114**, 7487–7556.

18. W. Lee, R. Ji, U. Gösele and K. Nielsch, *Nat. Mater.*, 2006, **5**, 741–747.

19. W. Lee and J.C. Kim, *Nanotechnology*, 2010, **21**, 485304.

20. W. Lee, R. Scholz and U. Gösele, *Nano Lett.*, 2008, **8**, 2155–2160.

21. W. Lee, J.C. Kim and U. Gösele, *Adv. Funct. Mater.*, 2010, **20**, 21–27.

22. K. Schwirn, W. Lee, R. Hillebrand, M. Steinhart, K. Nielsch and U. Gösele, *ACS Nano*, 2008, **2**, 302–310.

23. W. Lee, K. Schwirn, M. Pippel, R. Scholz and U. Gösele, *Nat. Nanotechnol.*, 2008, **3**, 234–239.

24. W. Cheng, M. Steinhart, U. Gösele and R.B. Wehrspohn, *J. Mater. Chem.*, 2007, **17**, 3493–3495.

25. M.S. Hunter and P. Fowle, *J. Electrochem. Soc.*, 1954, **101**, 481–485.

26. A. Santos, *J. Mater. Chem. C*, 2017, **5**, 5581–5599.

27. L.K. Acosta, F. Bertó-Roselló, E. Xifre-Perez, A. Santos, J. Ferré-Borrull and L.F. Marsal, *ACS Appl. Mater. Interfaces*, 2018, **11**, 3360–3371.

28. S.Y. Lim, C.S. Law, L.F. Marsal and A. Santos, *Sci. Rep.*, 2018, **8**, 9455.

29. S.E. Kushnir and K.S. Napolskii, *Mater. Des.*, **144**, 140–150.

30. L. Liu, S.Y. Lim, C.S. Law, B. Jin, A.D. Abell, G. Ni and A. Santos, *J. Mater. Chem. A*, 2019, **7**, 22514–22529.

31. Sukarno, C.S. Law and A. Santos, Nanoscale, 2017, 8, 7451–7550.

32. G. Macias, J. Ferré-Borrull, J. Pallarès and L.F. Marsal, *Nanoscale Res. Lett.*, 2014, **9**, 315.

33. T. Kumeria, A. Santos, M. M. Rahman, J. Ferré-Borrull, L. F. Marsal and D. Losic, *ACS Photonics*, 2014, **1**, 1298–1306.

34. G.D.Sulka and K. Hnida, *Nanotechnology*, 2012, **23**, 075303.

35. E. Yablonovitch, *Phys. Rev. Lett.*, 1987, **58,** 2059–2062.

36. S. John, *Phys. Rev. Lett.*, 1987, **58,** 2486–2489.

37. C. López, *Adv. Mater.*, 2003, **15,** 1680–1704.

38. J.E. Spanier and I.P. Herman, *Phys. Rev. B*, 2000, **61**, 10437–10450.

39. E. Lorenzo, C.J. Oton, N.E. Capuj, M. Ghulinyan, D. Navarro-Urrios, Z. Gaburro and L. Pavesi, *Appl. Opt.*, 2005, **44**, 5415–5421.

40. A. Santos, C.S. Law, T. Pereira and D. Losic, *Nanoscale*, 2016, **8**, 8091–8100.

41. S.O. Meade, M.S. Yoon, K.H. Ahn and M.J. Sailor, *Adv. Mater.*, 2004, **16**, 1811–1814.

42. H. Masuda, M. Yamada, F. Matsumoto, S. Yokoyama, S. Mashiko, M. Nakao and k. Nishio, *Adv. Mater.*, 2006, **18**, 213–216.

43. A.K. Tiwari, S. Shaik and S.A. Ramakrishna, *Appl. Phys. B*, 2018, **124**, 127.

44. C.S. Law, S.Y. Lim and A. Santos, *Sci. Rep.*, 2018, **1**, 4642.

45. L. Yisen, C. Yi, L. Zhiyuan, H. Xing and L. Yi, *Electrochem. Commun.*, 2011, **13**, 1336–1339.

46. S.Y. Lim, C.S. Lim, M. Markovic, J.K. Kirby, A. D. Abell and A. Santos, *ACS Appl. Mater. Interfaces*, 2018, **10**, 24124–24136.

47. S.Y. Lim, C.S. Law, M. Markovic, L.F. Marsal, N.H. Voelcker, A.D. Abell and A. Santos, *ACS Appl. Energy Mater.*, 2019, **2**, 1169–1184.

48. S.Y. Lim, C.S. Law, L. Liu, M. Markovic, A.D. Abell and A. Santos, *Catal. Sci. Technol.*, 2019, **9**, 3158–3176.

49. C.S. Law, S.Y. Lim, R.M. Macalincag, A.D. Abell and A. Santos, *ACS Appl. Nano Mater.*, 2018, **1**, 4418–4434.

50. C.S. Law, S.Y. Lim, A.D. Abell, L.M. Marsal and A. Santos, *Nanoscale*, 2018, **10**, 14139–14152.

51. A. Santos, C.S. Law, D.W.C. Lei, T. Pereira and D. Losic, *Nanoscale*, 2016, **8**, 18360–18375.

52. S.E. Kushnir, T.Y. Pchelyakova and K.S. Napolskii, J. *Mater Chem. C*, 2018, **6**, 12192–12199.

53. P. Yan, G.T. Fei, G.L. Shang, B. Wu and L. De Zhang, *J. Mater. Chem. C*, 2013, **1**, 1659–1664.

54. G.L. Shang, G.T. Fei, Y. Zhang, P.Yan, S.H. Xu and L. De Zhang, *J. Mater. Chem. C*, 2013, **1**, 5285–5291.

55. G. Shang, G. Fei, Y. Li and L. Zhang, *Nano Res.*, 2016, **9**, 703–712.

56. A. Santos, J.H. Yoo, C.V. Rohatgi, T. Kumeria, Y. Wang and D. Losic, *Nanoscale*, 2016, **8**, 1360–1373.

57. A. Santos, P. Formentín, J. Ferré-Borrull, J. Pallarès and L. F. Marsal, *Mater. Lett.*, 2012, **67**, 296–299.

58. Y. Wang, A. Santos, A. Evdokiou and D. Losic, *Electrochim. Acta*, 2015, **154**, 379–386.

59. D.C. Montgomery, *Design and Analysis of Experiments*, John Wiley & Sons Inc, New York, 2017.

60. M.D. Abràmoff, P.J. Magalhaes and S.J. Ram, *Biophotonics Int.*, 2004, **11**, 36–42.

61. A. Brzózka, A. Brudzisz, K. Hnida and G.D. Sulka, in *Electrochemically Engineered Nanoporos Materials: Methods, Properties and Applications*, ed. D. Losic and A. Santos, Springer, Switzerland, 2015, vol. 220, ch. 8, pp. 219–288.

62. G.L. Shang, G.T. Fei, S.H. Xu, P. Yan and L. De Zhang, *Mater. Lett.*, 2013, **110**, 156–159.

Nanoscale Accepted Manuscript